Electronic Supplementary Material (ESI) for Energy & Environmental Science.

Electronic supplementary information

Impact of Substrate Diffusion and Enzyme Distribution in 3D-Porous Electrodes: a combined electrochemical and modelling study of a thermostable H_2/O_2 Enzymatic Fuel Cell

Ievgen Mazurenko,[a] * Karen Monsalve,[a] Pascale Infossi,[a] Marie-Thérèse Giudici-Orticoni,[a] Frédéric Topin,[b] Nicolas Mano,[c] Elisabeth Lojou [a] *

[a] Aix Marseille Univ, CNRS, BIP, 31 chemin Aiguier, 13402 Marseille, France

[b] Aix-Marseille Univ, IUSTI-CNRS UMR 7343, Technopôle de Château Gombert, 5, Rue Enrico Fermi, Marseille Cedex 13 13453, France

[c] Centre de Recherche Paul Pascal, UPR 8641, CNRS, Bordeaux University, 33600 Pessac, France

* Corresponding authors: lojou@imm.cnrs.fr, imazurenko@imm.cnrs.fr

Measurement of *Bp* BOD apparent Michaelis constant

The planar pyrolytic graphite electrode (PG) covered with CNT layers and immobilized *Bp* BOD was used to estimate the apparent Michaelis constant at different potentials. First, the catalytic voltammograms were recorded at different O_2 partial pressures and rotation rates (Figure S1A). The blank-corrected values of the catalytic current at each potential were than plotted against rotation rate on the Koutecky-Levich plot (Figure S1B). Thus extrapolated to the infinite rotation rate catalytic currents at each O_2 partial pressure were fitted into Michaelis-Menten equation at each potential (Figure S1C). Found apparent Michaelis constant did not change at potentials lower than 0.35V and was 37±3 μM but seems to be lower at higher potentials (Figure S1D).

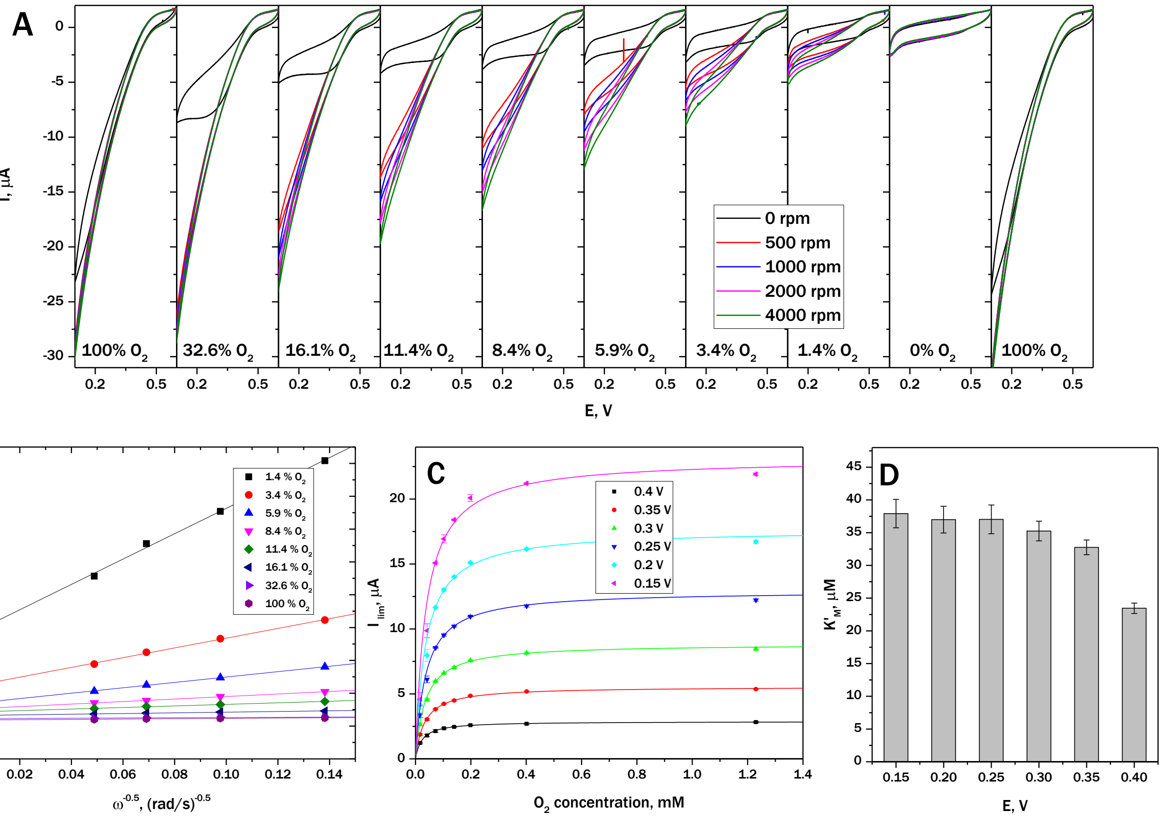

Figure S1. Measurement of Bp BOD apparent K'$_m$. (A) Cyclic voltammograms of PG-CNT-BOD at different partial pressures of O_2 and different rotation rates. Phosphate buffer pH 6, 0.2 M, scan rate 5 mV/s, 25 °C. (B) Example of Koutecky-Levich (at 0.3 V) plot used to estimate the catalytic current at infinite rotation rate (C) Fitting of the catalytic currents at infinite rotation rate and different potentials to Michaelis-Menten equation. (D) Estimated apparent Michaelis constants at different potentials.

Charge and species transport model in the EFC

Constitutive equations

Since extremely high currents were not expected to flow in the electrochemical cell, the electroneutrality condition can be assumed in the whole volume:

(1) $$\sum z_i c_i = 0$$

where z_i and c_i are charges and concentrations of current-carrying ions (sodium cations and phosphate anions from buffering solution).

At these conditions, the Nernst-Planck equation describing the mass-transfer of charge carriers, *i.e.* the current flow in the solution, simplifies to :

(2) $$i_l = -\frac{F^2}{RT}\nabla\varphi_l \sum z_i^2 D_i c_i = -\sigma_l \nabla\varphi_l$$

where D_i – diffusion coefficients of the charge-carrying species, $\nabla\varphi_l$ – gradient of solution potential, σ_l – solution conductivity, are assumed to be constant within all solution volume due to eletroneutrality condition.

The kinetics of an electrochemical reaction depends on the electrode potential which can be defined as a difference of the electrostatic potentials of electron-conducting phase (electrode, φ_s) and ion-conducting phase (electrolyte, φ_l) on the electrode-electrolyte boundary.

(3) $$E = \varphi_s - \varphi_l$$

The absolute values of these potentials being unmeasurable directly, only the potential difference between two electrodes can be accessed. The second electrode, *i.e.* the reference electrode is usually chosen to possess a constant potential $E_{REF} = \varphi_{s,REF} - \varphi_{l,REF} = const.$ At such conditions, the electrochemical potential of the electrode measured against the reference potential is expressed as:

(4) $$\Delta E_{E/REF} = \varphi_{s,E} - \varphi_{s,REF} = (\varphi_{s,E} - \varphi_{l,E}) - (\varphi_{s,REF} - \varphi_{l,REF}) + (\varphi_{l,E} - \varphi_{l,REF})$$

The term $(\varphi_{l,E} - \varphi_{l,REF})$ corresponds to the ohmic drop in the electrolyte solution which is equal to zero at no-current conditions and depends on the solution conductivity according to the equation (2) and on the distance between the two electrodes.

The bioelectrode kinetics measured experimentally in the conditions of substrate excess represents the dependence $i = f(\Delta E_{E/REF})$, and doesn't correspond to the real $i = f(E_E)$ enzymatic kinetics due to the significant current flow and perceptible expected ohmic drop. Furthermore, the bioelectrode kinetics obeys to the Michaelis-Menten enzymatic kinetics according to:

(5) $$i = nFv = nF\left(\frac{v_{max}c_s}{c_s+K'_m}\right) = \frac{i_{max}c_s}{c_s+K'_m}$$

Where v and v_{max} are the rate and the maximal rate of the enzymatic reaction, c_s is the enzymatic substrate concentration, K'_m – is the apparent Michaelis constant of the enzyme for this substrate, n – is the number of electrons transferred during conversion of one molecule of substrate.

The substrates of both enzymes being neutral dissolved gases, their diffusion is not influenced by electric field developed in the solution and (in the absence of convection) obeys to the Fick's second law equation:

(6) $$\frac{\partial c_s}{\partial t} = D_s \nabla^2 c_s$$

Inside the bioelectrode, the additional term appears which corresponds to the substrate consumption in the course of the enzymatic reaction:

(7) $$\frac{\partial c_s}{\partial t} = D_s \nabla^2 c_s - v$$

In the case of a porous electrode, both electron- and ion-conducting phases exist within the electrode volume. This extends significantly electrode-electrolyte boundary which can be described by specific surface area A_{sp} (m^2/m^3). Furthermore, the apparent diffusion rate of the ions is hindered since an ion should go a longer way to arrive from A to B due to the electrode fluid phase tortuosity τ. The same applies to the electrons in the solid phase of the porous electrode, yet the conductivity of the carbon being several order of magnitude higher then the electrolyte conductivity, this phenomenon can be often neglected. Taking into account both tortuosity and porosity (ε) of the porous media, the effective diffusion coefficient of the species can be calculated as:

(8) $$D_{eff,i} = \frac{\varepsilon}{\tau} D_i$$

The precise value of the tortuosity can be determined only from microscopic 3D-modelling of the pore distribution of the porous media. However, several empirical equations exist connecting tortuosity with electrode porosity. The model of Bruggeman is usually a good approximation for high values of porosity:[1]

(9) $$\tau = \varepsilon^{-1/2}$$

This gives:

(10) $$D_{eff,i} = \varepsilon^{3/2} D_i$$

Model 1: single bioelectrodes

In order to study factors governing bioelectrode performances, a 3D-model of the single-compartment electrochemical cell containing the reference and auxiliary electrodes was first constructed (Figure S2).

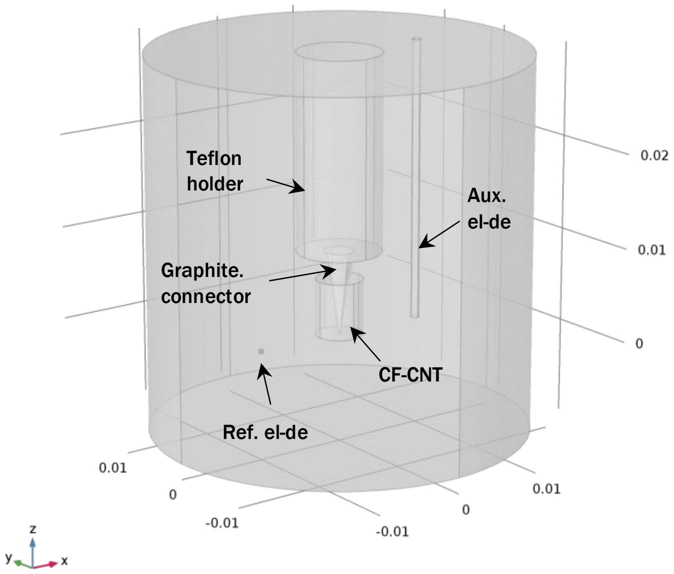

Figure S2. Geometry of the 3-electrode single cell used in the modelling

The CF-domain was meshed with tetrahedral elements with maximal size of 0.5 mm. In order to account for high concentration gradients expected on the border of the CF, sixteen layers of thin prismatic elements were added on each side of the CF/solution boundary. The mesh in the rest of the solution domain consisted of default tetrahedral elements. The Teflon holder and the graphite connector were excluded from the model and thus non-meshed.

The time-dependent solver with relative tolerance 0.0001 was used to simulate voltammograms in the range of times from 0 to 240 s (step 1 s) which corresponds to one cycle of CV with a scan rate of 5 mV/s.

Step 1. Defining ohmic drop inside porous electrode

Firstly, the model excluding mass-transfer was solved, *i.e.* only the equations (2), (4) and (10). This corresponds to the situation when the electrode rotates fast enough to compensate substrate depletion inside the porous media. The experimental i-E curves at 4000 rpm (Figure S9) were thus taken and interpolated in order to describe the electrochemical kinetics of the bioelectrode when given potential corresponds to $\Delta E_{E/REF}$. The results allow to estimate the ohmic drop inside the porous electrode and to deduce the real electrochemical kinetics of the bioelectrodes.

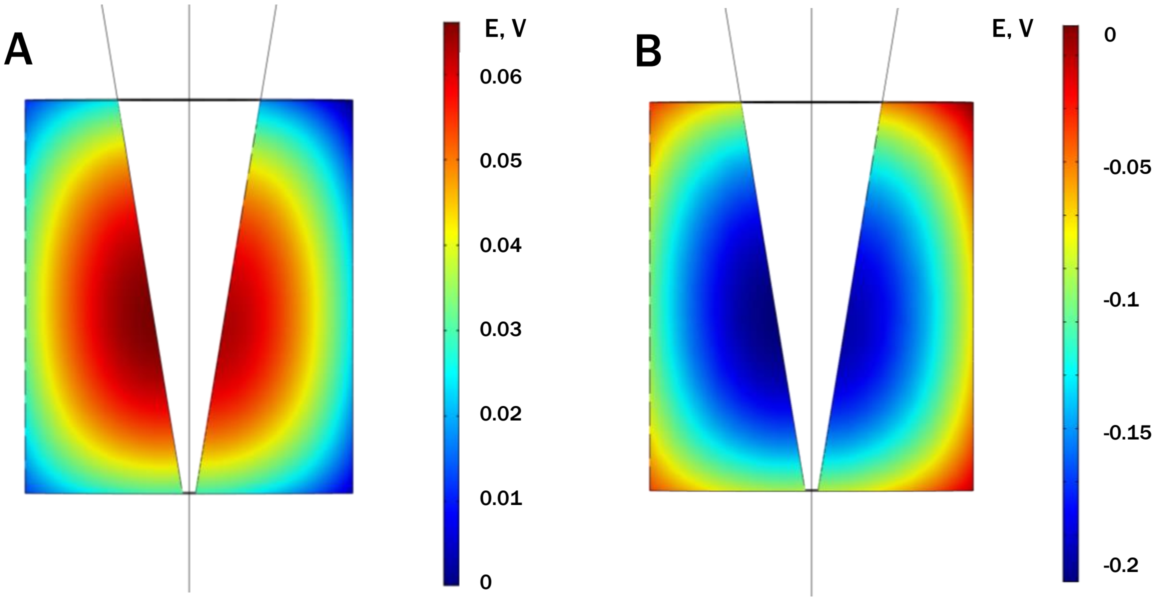

Figure S3. Cross-section view (along x-axis) of the distribution of the ohmic drop (calculated from the electrolyte potentials) inside (A) CF-CNT-*Aa* MBH and (B) CF-CNT-*Bp* BOD at maximal current densities, *i.e.* at $\Delta E_{E/REF}$=0 V.

Figure S3 shows that significant ohmic drop exists inside the bioelectrodes when currents close to 5 mA (anode) and 17 mA (cathode) pass. In these conditions the real potential of the anode interior is up to 65 mV lower than that one of the exterior, and the real potential of the cathode interior is up to 200 mV higher than on the exterior. These results allow to correct the bioelectrodes kinetics for the ohmic drop and to deduce the real i-E dependence (Figure S4):

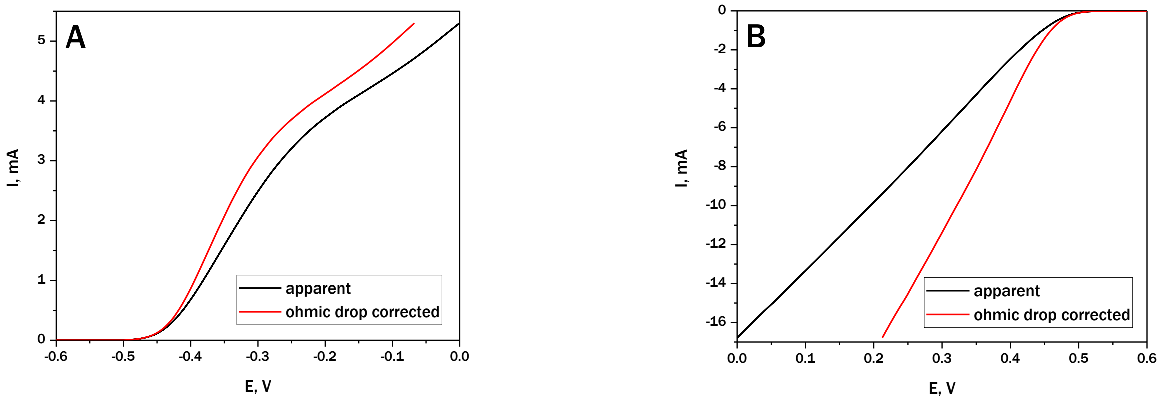

Figure S4. Experimental and ohmic drop corrected voltammograms of (A) CF-CNT-*Aa* MBH and (B) CF-CNT-*Bp* BOD.

Step 2. Validation of the model for diffusion-limited conditions.

The equations (2), (4) and (10) were further combined with equations (5) and (7), *i.e.* for the conditions when the bioelectrode kinetics is substrate-dependent and the mass-transfer of the latter occurs exclusively by diffusion (no convection conditions). Now, the real kinetics deduced at the step 1 was taken into account. The results are discussed in the main text (Figure 3). The brief influence of the ohmic drop inside the porous bioelectrode is visible notably on the Figure 3E leading to slightly faster oxygen consumption at the borders of the bioelectrode.

Model 2: enzymatic fuel cell

To study the bioelectrode performance in the optimal configuration a 2D-model of an EFC was constructed consisting of two bioelectrodes with thickness less than 1 mm and geometric square area 1 cm^2, separated by a separator of 0.18 mm thickness (corresponding to usual thickness of Nafion membrane). The bioelectrodes were assumed to be close enough to the gas phase, so that the quasi-equilibrium conditions ($c_s = c_{s,max}$ according to Henry's law) are always retained on the phase-boundary of the respective bioelectrodes. The rectangular mesh consisting of 50 elements geometrically-distributed so that the thickness of the closest to the phase boundary element is 10% of the thickness of the last one (Figure S5).

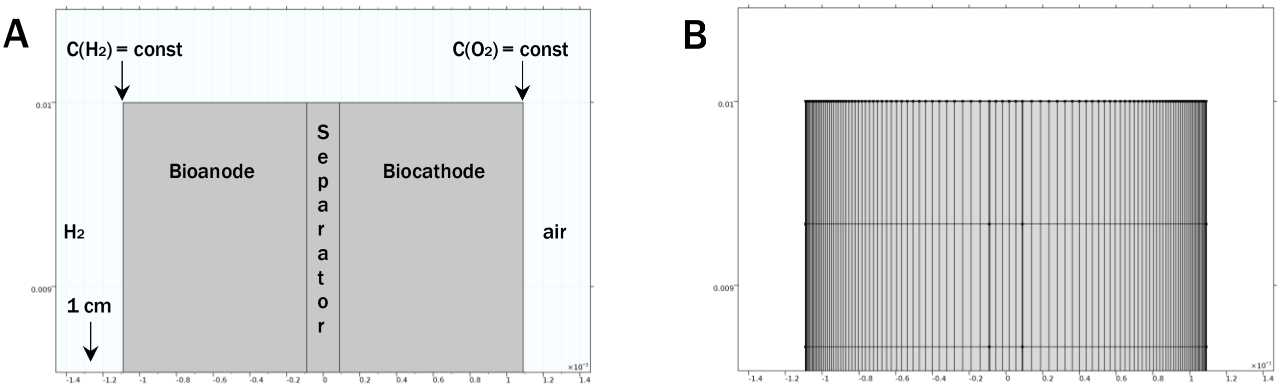

Figure S5. (A) Geometry and (B) meshing of the EFC domain.

The kinetic parameters of the bioelectrodes were taken from the Model 1 and the full set of the equations (2), (4), (5), (7), (10) was solved within the EFC domain. In the absence of the reference electrode, the electric potential of the cathode $\varphi_s$was chosen as a base and fixed to 0. In this case the electric potential of the anode was equal to the negative EFC voltage. The stationary solver (relative tolerance 10^{-7}) was used to solve the model at different cell voltages in the range 1.15 V – 0 V (step 0.05 V) giving the polarization curve.

In order to study the influence of the bioelectrode thickness (*d*) it was varied from 1000 to 10 μm (Figure S6). The maximal current and power density were first increasing and then stabilized at ca. 200-300 μm, approaching 0.85 mA/cm^2 and 0.35 mW/cm^2 respectively. Further thickness increase did not cause enhanced performance but rather a slight decrease. Indeed, at these thicknesses the kinetics of both electrodes starts to be limited by mass-transfer and the internal layers are deprived of the substrate (Figure

S6E-G). The ohmic drop increases as well resulting in slight decrease of the performances for thicker bioelectrodes (yet, being not significant, *e.g.* 10 mV for 1 mm thickness) (Figure S6C).

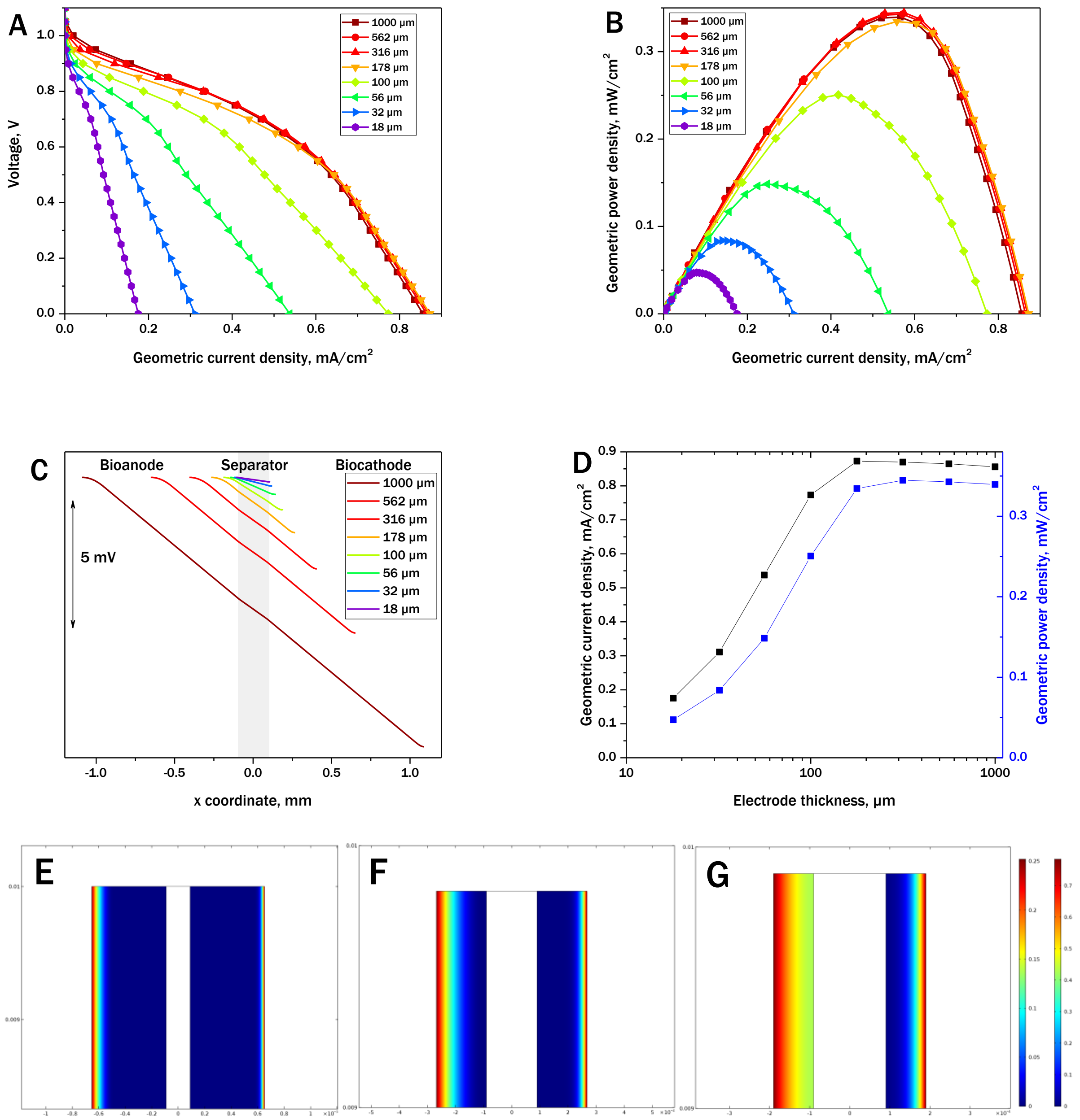

Figure S6. (A) Polarization curves and (B) Power density curves obtained with bioelectrodes with different thicknesses. (C) Electrolyte potential profile (*i.e.* ohmic drop) across X-axis at short circuit and different bioelectrodes thicknesses. (D) Maximal current and power density dependence on the bioelectrode thickness. (E-G) Distribution of H_2 (anode, left) and O_2 (cathode, right) concentration at maximal current density for the bioelectrodes of (E) 562 µm, (F) 178 µm and (G) 100 µm.

To study the influence of the electrode compression, an additional factor *q* was introduced, ranging from 1 to 9 (1 – no compression; 9 – electrode compressed 9 times). The electrode material was assumed to be incompressible, *i.e.* only the pore volume was affected. Accordingly, the compression was influencing the electrode thickness, porosity and specific surface area according to:

$$d = {}^{d_0}\!/_{q};\quad A_{sp} = qA_{sp}^{0};\quad \varepsilon = 1 + q\varepsilon^{0} - q \tag{11}$$

Figure S7 shows the results of the compression study. The initial bioelectrode thickness was 250 µm, *i.e.* close to the optimal one determined on the previous step. It appears that 1.5 times increase of the maximal current (1.3 mA/cm^2) and power density (0.5 mW/cm^2) can be obtained if the bioelectrodes were compressed further *ca.* 4 times that corresponds to a thickness of 63 µm and an apparent porosity of 0.6. In all cases the substrate mass-transfer seems to be a major limiting factor since no significant ohmic drop (less than 10 mV) is observed in the EFC.

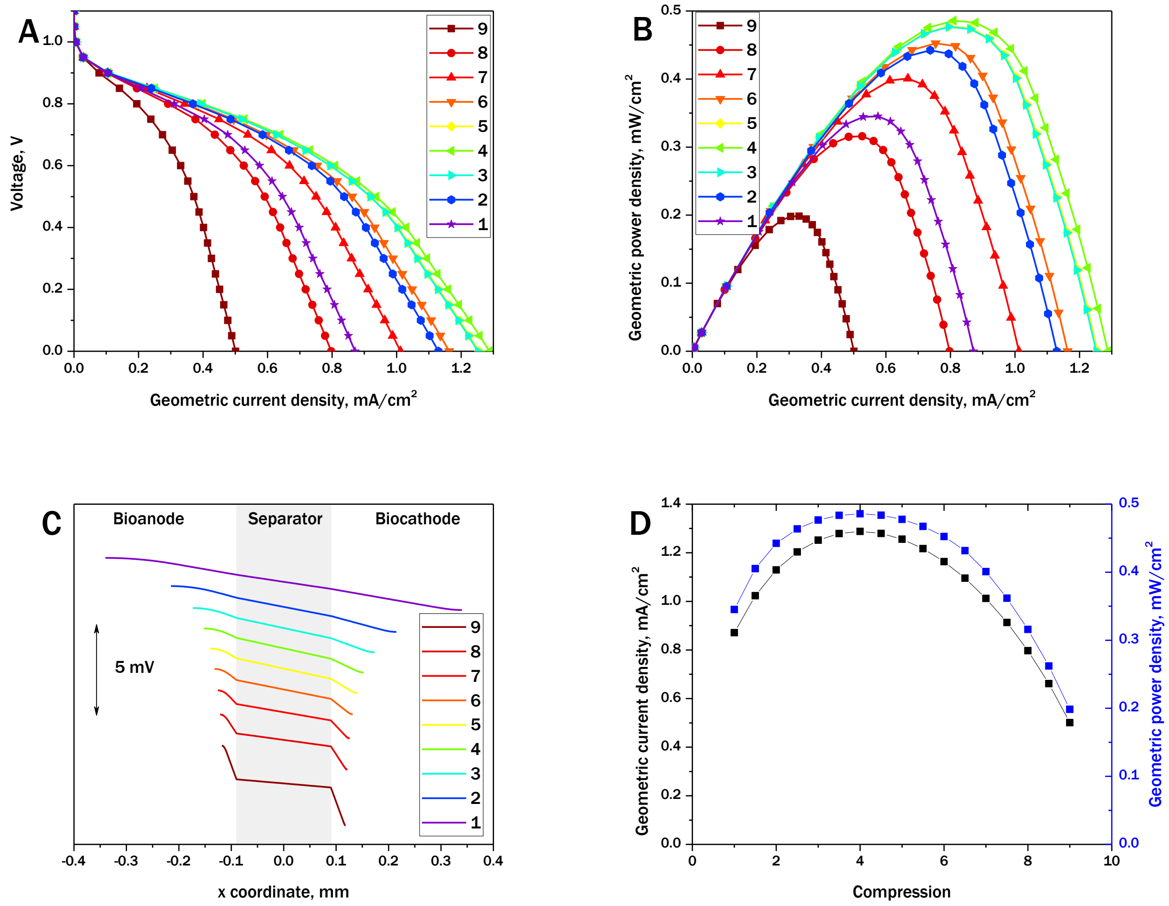

Figure S7. (A) Polarization curves and (B) Power density curves obtained with bioelectrodes compressed several times. (C) Electrolyte potential profile (*i.e.* ohmic drop) across X-axis at different compression factors and short circuit. (D) Maximal current and power density dependence on the compression factor.

Some other parameters used in the models are mentioned in the following table:

Parameter	Value	Description
T	298 K	Temperature
P	1 bar	Pressure
v	0.005 V/s (Model 1)	Scan rate
ε	0.9 (Model 1) $1 - 0.1q$ (Model 2)	Porosity
D_{H_2}	$4.5 \cdot 10^{-9}$ m²/s	Hydrogen diffusion coefficient
$c_{H_2}^{max}$	0.784 mol/m³	Saturated hydrogen concentration at 1 bar
$K_M^{Aa\ MBH}$	0.003 mol/m³	Apparent Michaelis constant *Aa* MBH
$K_M^{Bp\ BOD}$	0.037 mol/m³	Apparent Michaelis constant *Bp* BOD
D_{O_2}	$2.1 \cdot 10^{-9}$ m²/s	Oxygen diffusion coefficient
$c_{O_2}^{max}$	1.2 mol/m³ (Model 1) 0.252 mol/m³ (Model 2 - air)	Saturated oxygen concentration at 1 bar
σ_l	2 S/m	Phosphate buffer conductivity
σ_s	$1 \cdot 10^5$ S/m	Carbon conductivity
A_{sp}	$9 \cdot 10^5$ m^{-1} q × $9 \cdot 10^5$ m^{-1}	Specific surface area of CF-CNT

Material characterization

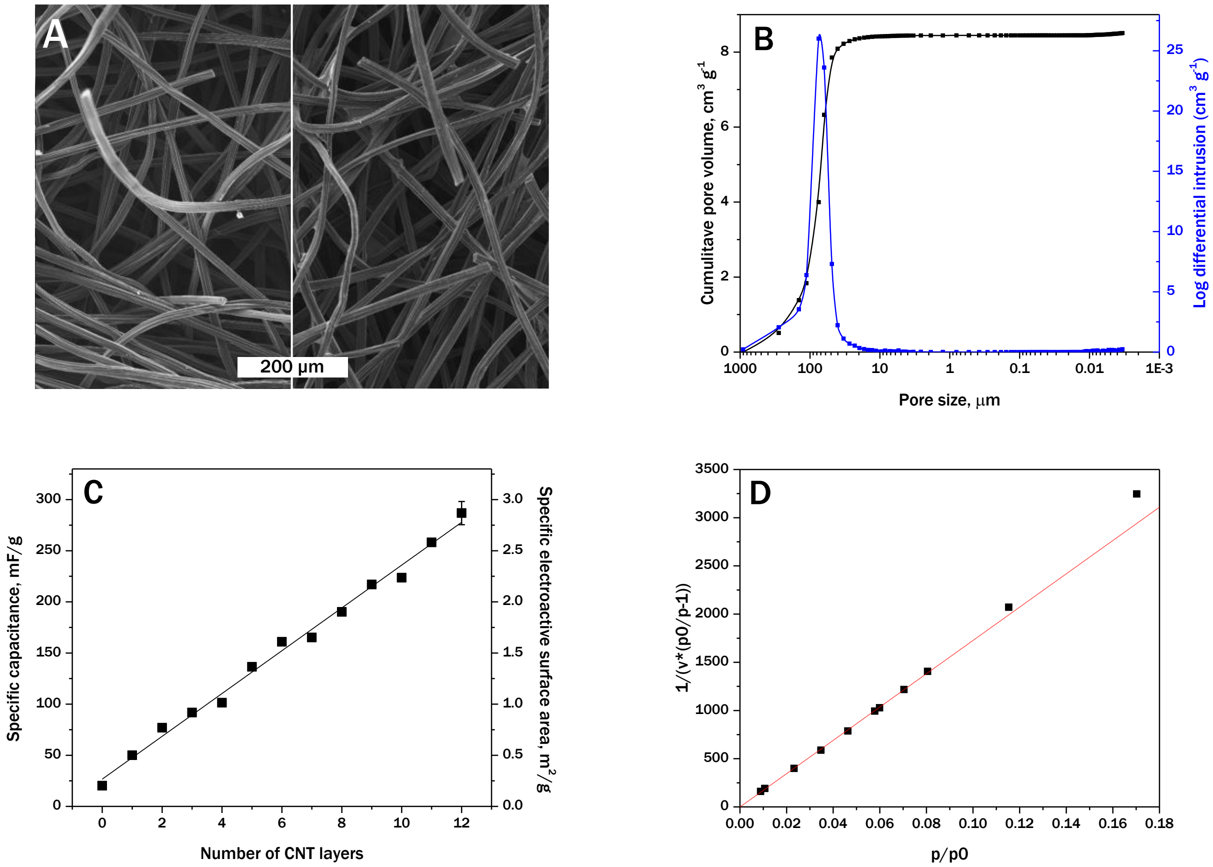

Figure S8. (A) SEM images with magnification 300x of CF (left) before and (right) after modification with CNTs; (B) Cumulative and differential mercury intrusion volume of CF; (C) Capacitance and deduced electroactive surface area of CF-CNT as a function of number of CNT-layers (last point – SD for 10 different CF); (D) BET plot of CF-CNT

As expected from high porosity, both electrodes do not exhibit high BET specific surface area: 2.1 and 5.6 $m^2 g^{-1}$ for CF and CF-MWCNT respectively as determined from BET-plot at low partial pressures (Figure S8D). Interestingly, the BET surface of CF-MWCNT is only 2.5 times larger than the surface of CF, whereas the ratio of 15 was observed by capacitance measurement (Figure S8C). The difference might lie in different approaches used for measurements: while N_2 molecules penetrate well into the smallest micropores, the solvated electrolyte ions have difficulties to penetrate inside the pores smaller ca. 1 nm resulting in the smaller specific area always obtained from capacitance measurements. In support of this, estimated from mercury porosimetry CF surface area that included pores larger than ca. 13 nm was found 0.5 $m^2 g^{-1}$, i.e. much smaller than BET surface area. Taking into account the absence of noticeable mesopores on the N_2 adsorption isotherm, the difference 1.6 $m^2 g^{-1}$ may be attributed to the micropores not assessable by mercury porosimetry nor capacitance measurements. Thus, the specific surface area of the electrode (microporosity excluded) was increased from 0.5 to 4 $m^2 g^{-1}$ by modification by MWCNTs constituting a factor of 8, i.e. close to the surface area estimated by capacitance measurements.

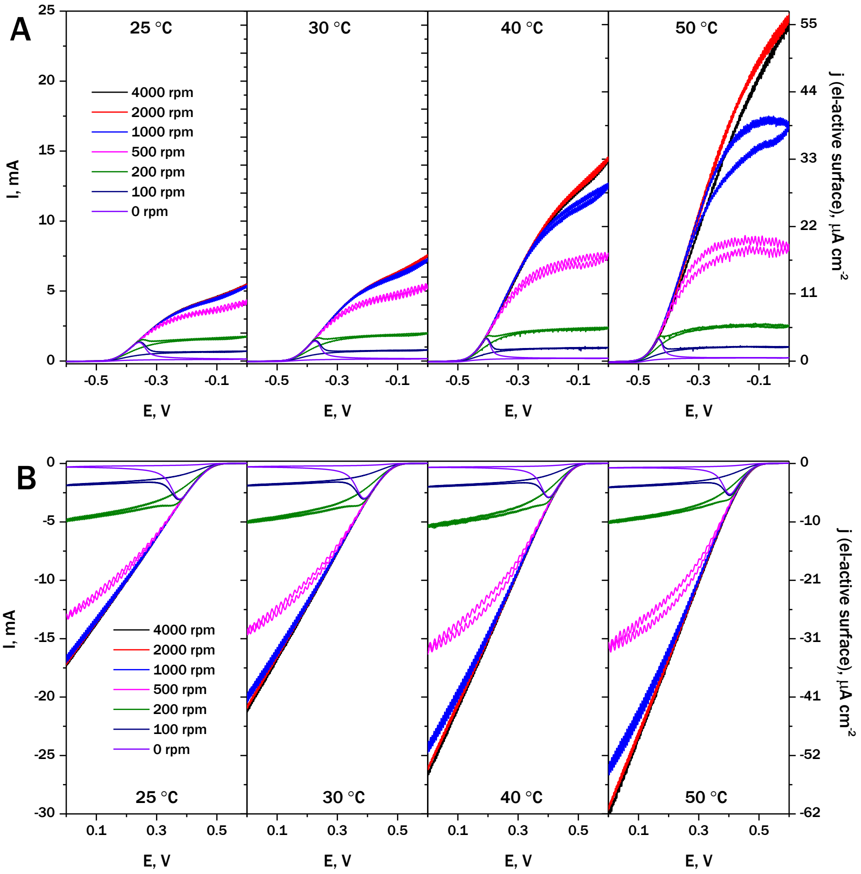

Figure S9. Catalytic CVs of (A) CF-CNT-*Aa* MBH (total quantity added 1.48 nmol) under 100% H_2 and (B) CF-CNT-*Bp* BOD (total quantity added 4.12 nmol) under 100% O_2 atmosphere at different temperatures and rotation rates. Phosphate buffer pH 6, 0.2 M, scan rate 5 mV s^{-1}.

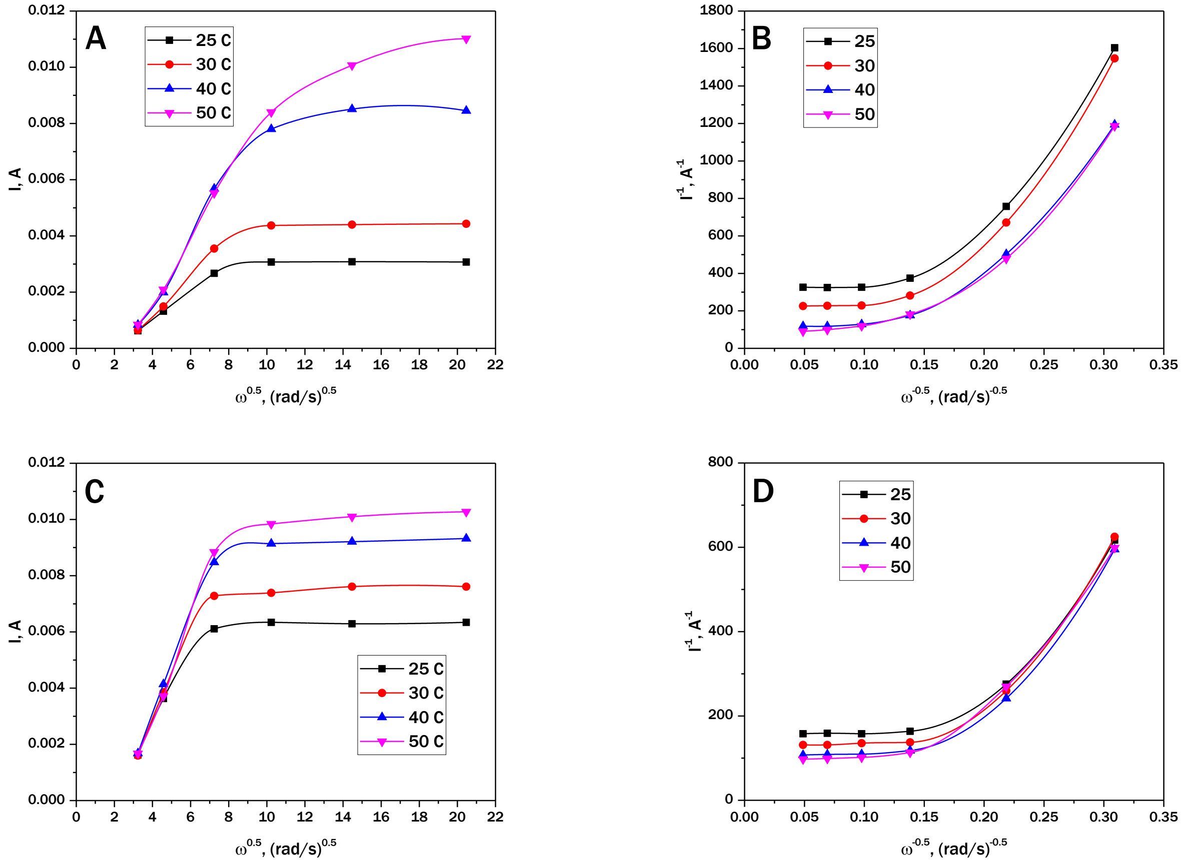

Figure S10. (A, C) Levich and (B,D) Koutecky-Levich plots of (A,B) CF-CNT-*Aa* MBH and (C,D) CF-CNT-*Bp* BOD catalytic currents at -0.3 V and 0.3 V respectively.

Bioelectrode stability

The operational stability of the bioelectrodes was evaluated in the potentiostatic mode at 25 °C during several days of functioning in substrate-reach conditions (Figure S11). The catalytic currents were intentionally made not very high in order to probe true enzymatic kinetics not influenced by mass-transfer. Assuming the first-order kinetics of the enzyme deactivation as a function of enzyme amount ($\partial[E]/\partial t = -k[E]$), the process can be described by the exponential decay equation $I = I_0 e^{-kt}$. The resulting chronoamperometric curves were fitted to this equation giving the parameter k of $4.25 \cdot 10^{-3}$ h^{-1} and $1.09 \cdot 10^{-3}$ h^{-1} for *Bp* BOD and *Aa* MBH respectively (Figure S11). This allows to estimate enzyme half-life according to $t_{1/2} = \ln(2)/k$, resulting in 163 h for *Bp* BOD and 639 h for *Aa* MBH.

In order to estimate total turnover number of the enzyme (TON), the exponential decay equation for each enzyme was integrated from t = 0 to ∞, thus giving total charge (and amount of the substrate converted) passed until the enzyme is completely deactivated. The total amount of the enzyme converted was further divided by the amount of the enzyme at t = 0, estimated from the current and turnover constants of both enzymes at a given potential previously defined in the text. The obtained values of TON were $9.6 \cdot 10^5$ (total amount of enzyme) and $1.1 \cdot 10^7$ (amount of electroactive enzyme) for *Bp* BOD, $8.9 \cdot 10^7$ (total amount of enzyme) and $6.3 \cdot 10^8$ (amount of electroactive enzyme) for *Aa* MBH.

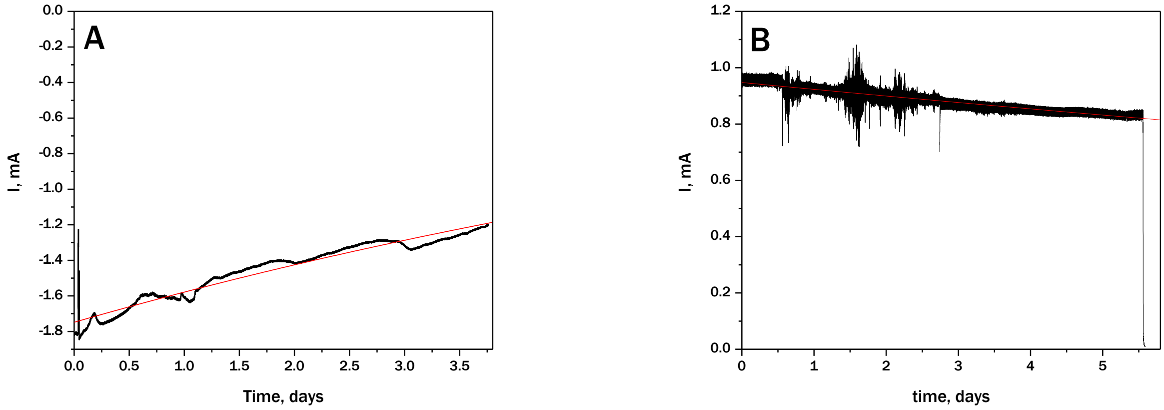

Figure S11. (A) Stability of the CF-CNT-*Bp* BOD catalytic response in the potentiostatic mode. Applied potential 0.328 V, Phosphate buffer pH 6 0.1 M, 1000 rpm, ca. 25 °C, O_2 atmosphere; (B) Stability of the CF-CNT-*Aa* MBH catalytic response in the potentiostatic mode. Applied potential -0.3 V, Phosphate buffer pH 7 0.2 M, 1000 rpm, 25 °C, H_2 atmosphere; Red lines represent zero-offset monoexponential fit of the curves.

Verification of enzyme distribution

In order to verify if the enzyme is homogeneously distributed within the entire CF-CNT volume, the modified CF-CNT-*Aa* MBH was cut along the polar axis into two unequal cylinders (*ca.* 2:3 size ratio). Figure S12A shows catalytic responses of the initial CF-CNT-*Aa* MBH and of the two resulting pieces. Once normalized to the electroactive surface area derived for each electrode from the capacitance measurements, all three electrodes give the same value of the catalytic current (Figure S12B). This suggests that the enzyme molecules are homogenously distributed over the electrode volume and equally occupy the available electroactive surface.

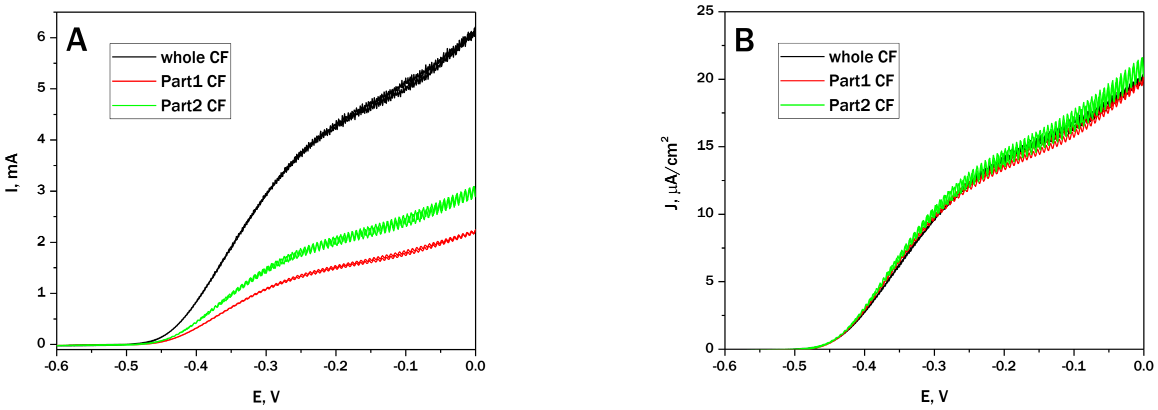

Figure S12. (A) Catalytic voltammograms of (black line) initial CF-CNTs-*Aa* BOD, and (red and green lines) two unequal parts obtained after cutting the initial electrode along the polar axis. (B) The same catalytic curves normalized for internal electroactive area of the respective electrodes. Phosphate buffer pH 6 0.2 M, (black line) 2000 rpm and (red and green lines) 1000 rpm, 25 °C, H_2

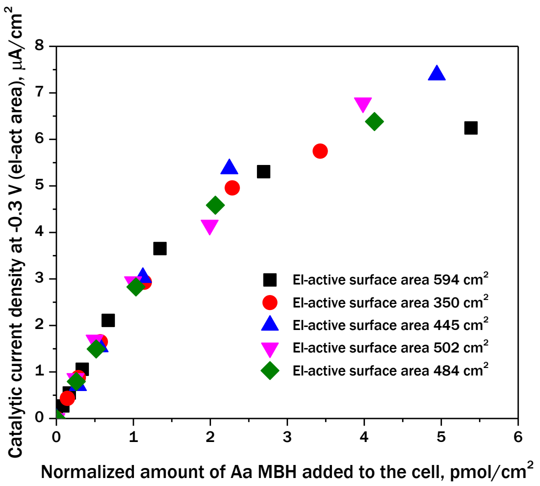

Figure S13. Pseudo-isotherms of *Aa* MBH adsorption on CF-CNTs with different quantities of CNTs and electroactive surface area. Both currents and added enzyme amounts are normalized to the electrode electroactive surface area. Phosphate buffer 0.2 M, cell volume 10 mL, 1000 rpm, 25 °C, H_2

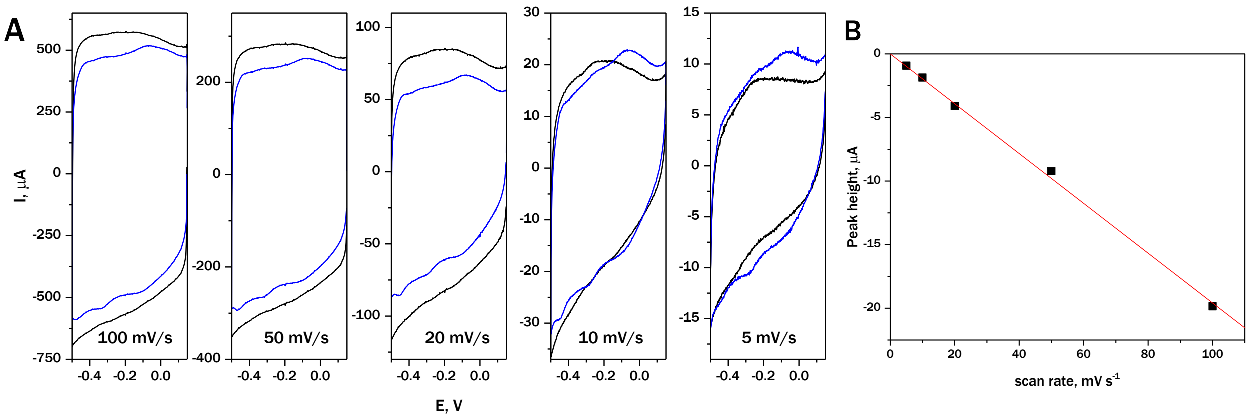

Figure S14. (A) Cyclic voltammograms of CF-CNT at different scan rates under N_2 atmosphere here (black lines) before and (blue lines) after adsorption of *Aa* MBH (1.43 nmol added to the cell). Phosphate buffer pH 7 0.2 M, 0 rpm, 25 °C. (B) Scan rate dependence of the peak at -0.27 V.

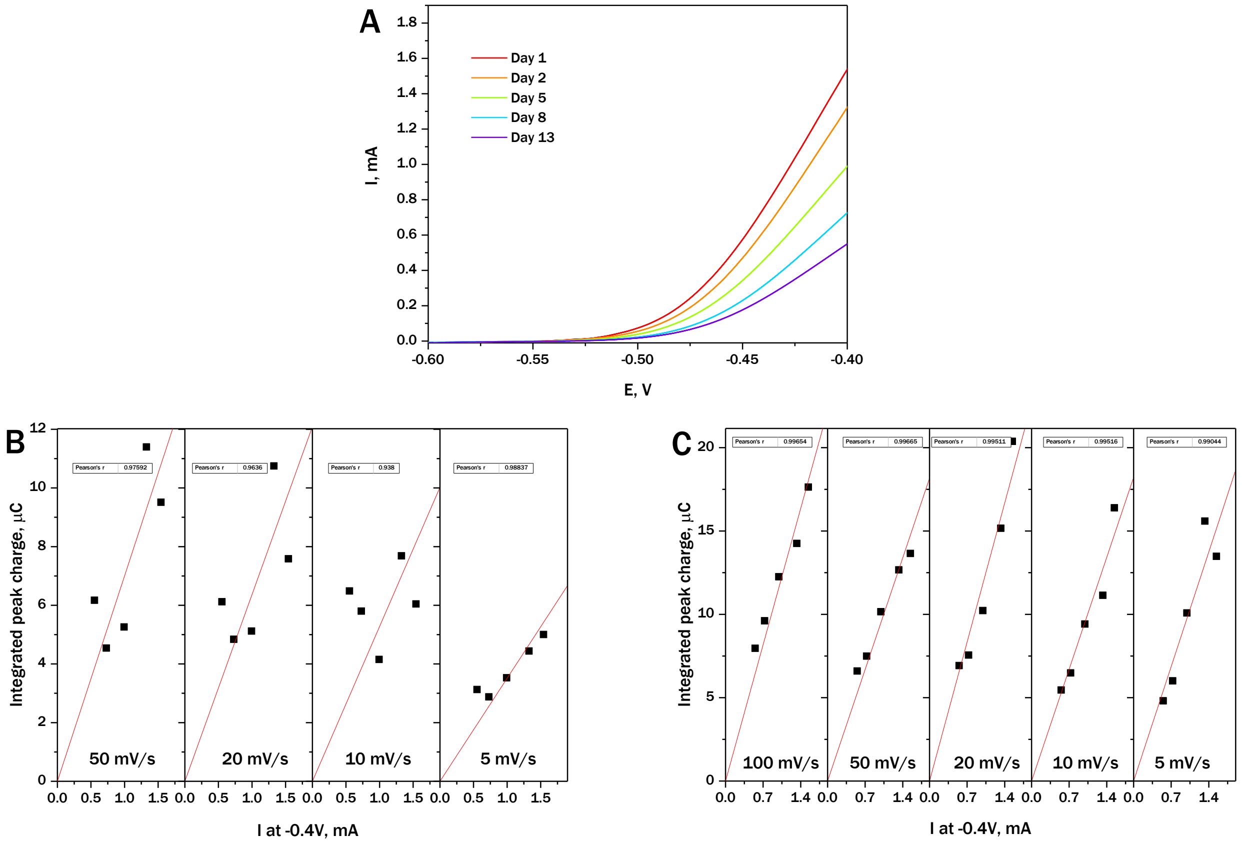

Figure S15. (A) Catalytic curves of CF-CNT-*Aa* MBH left in the cell at different days; Phosphate buffer pH 7 0.2 M, 1000 rpm, 25 °C, scan rate 5 mV s^{-1}, 100% H_2 atmosphere; (B, C) Correlation of the peaks at (B) -0.45 V and (C) -0.29 V via the integral intensity at different scan rates with the catalytic current observed during the deactivation experiment.

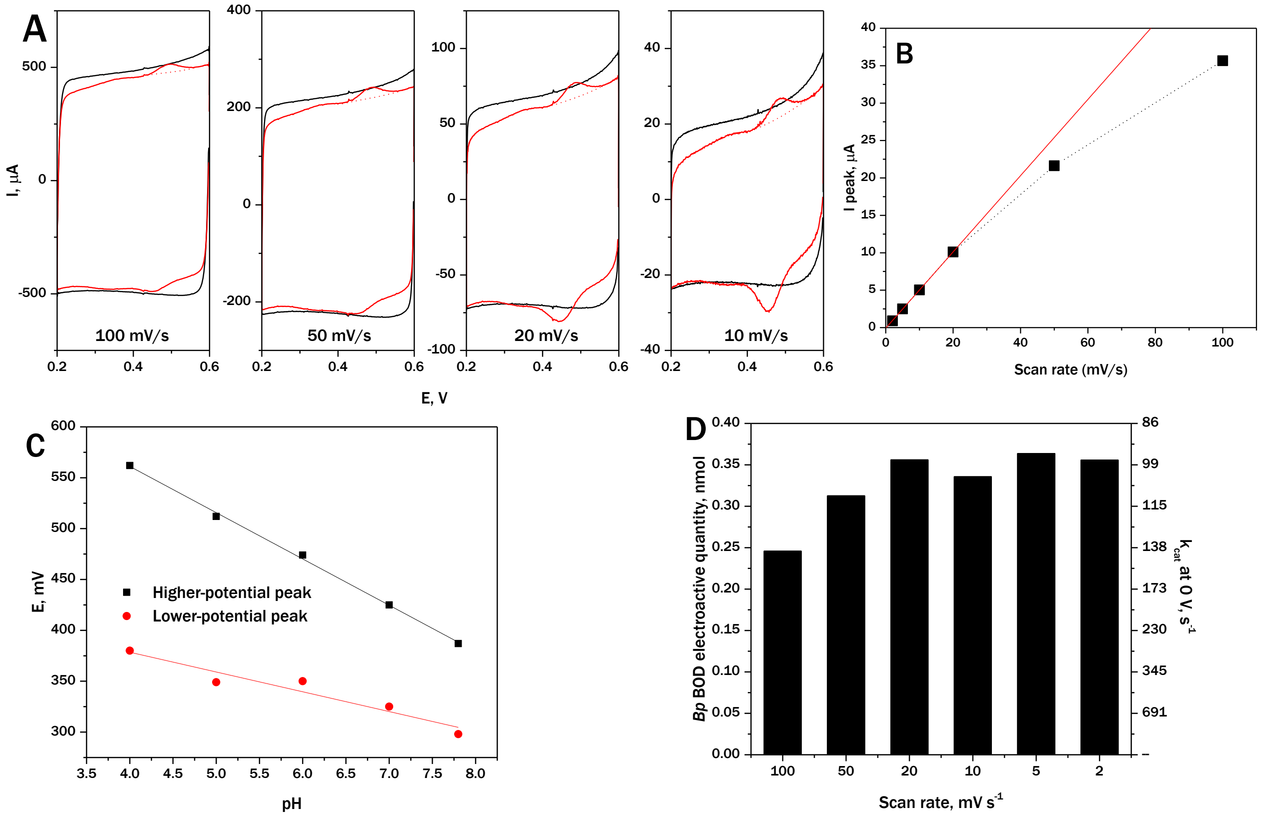

Figure S16. (A) Cyclic voltammograms of CF-CNT at different scan rates under N_2 atmosphere (black lines) before and (red lines) after adsorption of *Bp* BOD (4.12 nmol added to the cell). Phosphate buffer pH 6 0.2 M, 0 rpm, 25 °C; (B) Scan rate dependence of the peak at 0.47 V (C) Potential pH-dependence of the two visible peaks on the SWV. (D) The amount of electroactive *Bp* BOD obtained by the integration of the anodic peak at 0.47 V at different scan rates and corresponding turnover constants calculated from the catalytic current values at 0 V.

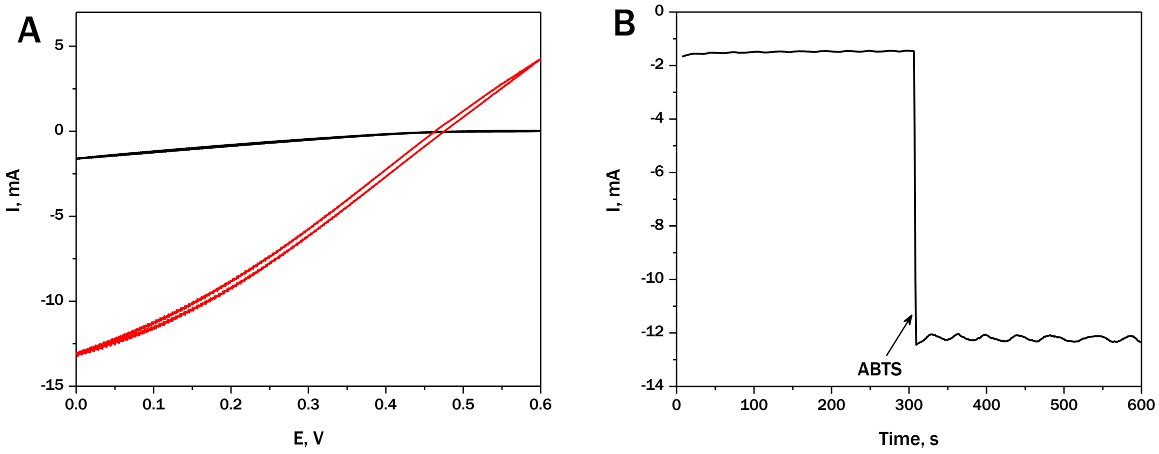

Figure S17. (A) Cyclic voltammograms of CF-CNT-*Bp* BOD (half-size: 5 x 3 mm) under O_2 atmosphere (black lines) before and (red lines) after addition of 1 mM ABTS. (B) Chronoamperogram of CF-CNT-*Bp* BOD (half-size: 5 x 3 mm) under O_2 atmosphere at 0 V during the addition of 1 mM ABTS. Phosphate buffer pH 6 0.2 M, 2000 rpm, 4 °C.

Supplementary references:

1. D.-W. Chung, M. Ebner, D. R. Ely, V. Wood and R. Edwin García, *Model. Simul. Mater. Sci. Eng.*, 2013, 21, 074009.